ADVANCED FUNCTIONAL MATERIALS
www.afm-journal.de

"Chemical Weathering" Exfoliation of Atom-Thick Transition Metal Dichalcogenides and Their Ultrafast Saturable Absorption Properties

Gang Zhao, Shuo Han, Aizhu Wang, Yongzhong Wu, Mingwen Zhao, Zhengping Wang,* and Xiaopeng Hao**

2D transition metal dichalcogenides are attracting increased attention because of their excellent electronic and optical properties. Inspired by the natural weathering exfoliation of seaside rocks, a "chemical weathering" concept for fabricating atom-thick 2D materials from their bulk counterparts is proposed. It is experimentally demonstrated that chemical weathering-assisted exfoliation mechanism is a simple and efficient method of preparing atom-thick MoS_2 and WS_2 monolayers. These monolayers are difficult to prepare using other approaches. Interestingly, the as-prepared MoS_2 and WS_2 monolayers exhibit excellent saturable absorption and mode-locking properties in all-solid-state lasers because of intermediate states resulting from S-vacancy defects. The obtained passively Q-switched laser operation with 60 ns pulse width and ultrafast mode locking with 8.6 ps pulse width are promising for all-solid-state laser application.

1. Introduction

2D layered nanomaterials such as graphene and transition metal dichalcogenide (TMD) nanosheets are receiving significant research attention in recent years because of their unique dimensionality effect and excellent physical and chemical properties.[1–15] High-quality large-area graphene has been successfully used as saturable absorbers in fiber and bulk solid-state lasers to generate Q-switched or mode-locked ultrafast pulses.[16–19] Subsequently, 2D topological insulators such as Bi_2Te_3, Bi_2Se_3, and Sb_2Te_3 have also been investigated in the field.[20–23] These works impel further studies on other 2D materials.

Q-switching and mode locking of fiber lasers with MoS_2 have been achieved early this year.[24,25] MoS_2 exhibits improved saturated absorption response compared with graphene under similar excitation condition;[12] thus, MoS_2 can be potentially used as a saturable absorber in solid-state lasers. Wang et al. synthesized an ultrathin MoS_2 film containing 30 layers through pulsed laser deposition (PLD) and obtained passive Q-switching with a pulse width of 410 ns.[26] This finding confirms the plausibility of using MoS_2 in solid-state lasers. However, mode locking and fine Q-switching remain unattainable; in these phenomena, the generation of ultrafast high-energy solid-state laser pulses requires an atomic thick and robust MoS_2, which exhibits rapid optical–electronic responses and high antidamage threshold. This type of material is difficult to prepare using conventional PLD method.

Atom-thick 2D materials can be produced through exfoliation approaches. Graphene obtained through exfoliation is relatively perfect and mature.[27] Other 2D materials such as TMDs are difficult to exfoliate through chemical methods because they easily react with acid and oxygen. Thus far, ultrathin TMDs can only be synthesized using micromechanical exfoliation[28,29] or chemical vapor deposition.[30] However, the former provides low yield, while the latter is an expensive method, and both of them produce TMDs with uncontrollable thickness. Therefore, an efficient approach to synthesize atomic-thin TMDs must be developed.

On the basis of the natural weathering exfoliation of seaside rocks (Figure S1, Supporting Information), we propose a "chemical weathering" concept for exfoliation of atom-thick 2D materials from their bulk counterparts. By performing a series of experiments combined with first-principles calculations, we demonstrated that the proposed exfoliation mechanisms based on "chemical weathering" can efficiently synthesize monolayers of TMDs such as MoS_2 and WS_2 under alkaline conditions. We initially verified that the as-prepared MoS_2 and WS_2 monolayers exhibit excellent mode-locking property in all-solid-state lasers because tunable intermediate states exist within the band gap. This study is the first to achieve saturable absorption and mode locking in WS_2, which are superior to those of MoS_2. In comparison with other approaches,[31,32] "chemical weathering" is a simple, universal, cheap, and efficient method and can be applied to exfoliate a wide range of layered materials, such as graphite and hexagonal boron nitride (Figures S2 and S3, Supporting Information).

Dr. G. Zhao, Dr. S. Han, Dr. A. Wang, Prof. Y. Wu,
Prof. M. Zhao, Prof. Z. Wang, Prof. X. Hao
State Key Lab of Crystal Materials
School of Physics
Shandong University
Jinan 250100, P.R. China
E-mail: zmw@sdu.edu.cn; zpwang@sdu.edu.cn;
xphao@sdu.edu.cn

DOI: 10.1002/adfm.201501972

2. Results and Discussion

In the process of natural chemical weathering, salts and alkali solution can erode the surface and permeate into the interlayer of rocks. The evaporation of water causes the crystallization of the solution, resulting in the dislocation and exfoliation of the rock stratum. After this process occurs repeatedly, soil is formed.

On the basis of this natural phenomenon, we aim to exfoliate TMD crystals into monolayers via the "chemical weathering" mechanism. In our experiments, exfoliation under alkaline conditions is related to inserting concentrations of cations (Na^+) and anions (OH^-) into the interlayer space. A low concentration of NaOH solution may fail to overcome the van der Waals (vdW) interlayer interactions to exfoliate the bulk materials. Moreover, the corrosion of the edges of the raw materials under NaOH solution facilitates the infiltration of Na^+ and OH^- into the interlayer space and subsequently results in NaOH crystallization. Hence, a suitable concentration of NaOH solution is important.

To determine the suitable NaOH concentration, we performed first-principles calculations based on density functional theory (DFT) (**Figure 1**f,g). The variation of the interlayer binding energy as a function of the interlayer spacing was used to describe the feasibility of exfoliating MoS_2 and WS_2 bulk crystals under NaOH solution. Figure 1f shows that the interlayer interaction at the equilibrium state (d = 5.965 Å for MoS_2 and d = 6.216 Å for WS_2) exhibited the energies of −0.726 (MoS_2) and −0.614 eV per atom (WS_2) without NaOH insertion. The interlayer distances increased to d = 7.915 Å (MoS_2) and d = 7.965 Å (WS_2) at the equilibrium state when the NaOH concentration in MoS_2 and WS_2 crystals was higher than 7.6% (one NaOH pair per four MoS_2 or WS_2 pairs). As a result, the interaction among the adjacent TMD layers declined at these interlayer distances. Therefore, when the NaOH is removed from the interlayer space, the bulk TMD crystals are exfoliated into ultrathin lamellas.

Considering this analysis, we propose a layer-by-layer mechanism based on chemical weathering to exfoliate MoS_2 and WS_2 nanosheets under alkaline conditions. (1) The chemically reactive edges and steps of the raw materials are first corroded under NaOH solution. The adsorption of Na^+ ions on the topmost surface causes buckling particularly in the region near the edges.[31] This condition facilitates subsequent infiltration of Na^+ and OH^- into the interlayer space of MoS_2 or WS_2 crystal. (2) As a result of the high chemical potentials of Na^+ and OH^- in the solution, the infiltration of Na^+ and OH^- into the interlayer space of MoS_2 or WS_2 crystal continuously occurs and leads to the accumulation of NaOH in the raw materials. (3) The crystallization of NaOH enlarges the interlayer spacing of the bulk materials and thus facilitates subsequent infiltration. (4) When the concentration of NaOH in MoS_2 or WS_2 crystal exceeds the critical value (≈7.6%) by repeating (2) and (3) processes, the raw materials are eventually exfoliated into ultrathin pieces.

Scanning electron microscopy (SEM) was used to study the morphologies of the as-obtained products dispersed in ethanol solution (Figure 1c,d). Ultrathin MoS_2 nanosheets were produced as shown in Figure 1c. These nanosheets exhibited sizes ranging from 500 nm to 1 µm. And large-sized (1–2 µm) ultrathin WS_2 nanosheets are shown in Figure 1d. Their morphology significantly differed from that of the raw materials (Figure 1a,b). These results clearly indicated that ultrathin MoS_2 or WS_2 nanosheets can be fabricated using the "chemical weathering" method.

To determine the effect of "chemical weathering" exfoliation on the phase structures of MoS_2 and WS_2, we recorded the XRD patterns, differential reflectance spectra, and Raman spectra of the raw materials and as-produced nanosheets (as shown in Sections S6 and S7 in the Supporting Information).

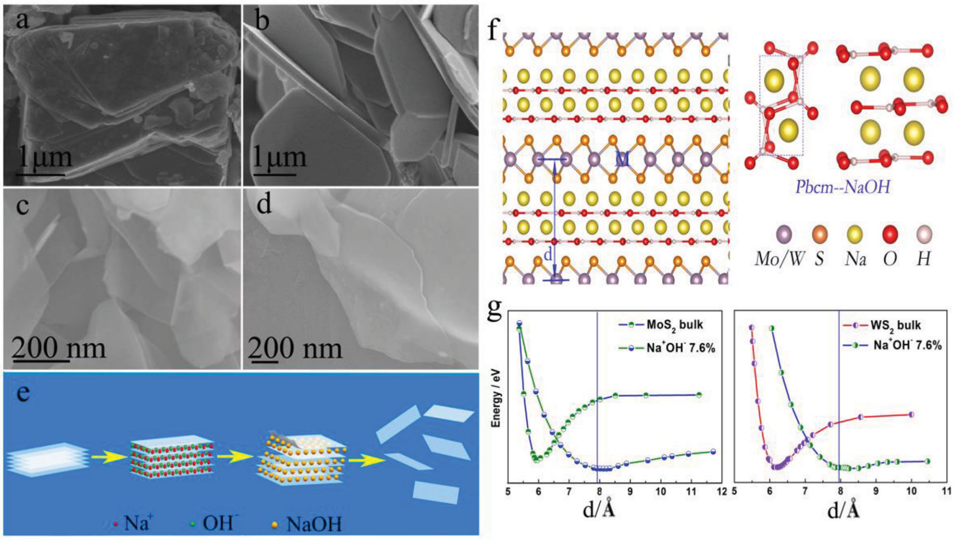

Figure 1. a,b) SEM images of MoS_2 and WS_2 raw materials. c,d) SEM images of "chemical weathering" exfoliation of monolayer MoS_2 and WS_2 nanosheets. e) Schematic illustration of "chemical weathering" exfoliation of monolayer MoS_2 and WS_2 nanosheets. f) Schematic illustration of exfoliation of a theoretical model with NaOH. g) Interlayer binding energy as a function of d (Å) for the bulk materials and a specific concentration of NaOH into the interlayer space of the bulk materials. The letter d (Å) represents the distance between the layers.

These findings implied that the crystal structures of the raw materials were well preserved during the exfoliation process. Furthermore, WS_2 possessed many characteristics similar to those of MoS_2.[6,33,34] Moreover, MoS_2 or WS_2 nanosheets exhibited good dispersibility and high solubility in water and ethanol solutions. The Tyndall effect was also evident under red-laser irradiation (Figure S8, Supporting Information).

Transmission electron microscopy (TEM) analysis of ultrathin MoS_2 and WS_2 nanosheets was performed (Figure S9a,b, Supporting Information). Typical 2D flakes consisting of ultrathin nanosheets and numerous nanosheets (MoS_2 and WS_2) were observed. The lateral size of these objects ranged from 500 nm to 2 µm, which is in accordance with the SEM results. The electron diffraction patterns of MoS_2 and WS_2 nanosheets are demonstrated in the insets of Figure S9a,b (Supporting Information). These patterns illustrated the hexagonal symmetry of MoS_2 and WS_2 materials. Moreover, Figure S9c,d (Supporting Information) shows that the whole structures of MoS_2 and WS_2 nanosheets were not destroyed during exfoliation. Interestingly, vacancy defects were observed in the ultrathin nanosheets particularly in the region near the edges as shown in **Figure 2**a–d.

The atomic ratios of the raw materials using the XPS spectra (Figure S10, Supporting Information) and found that these ratios were S/Mo = 2.035 and S/W = 2.024. These results were satisfactory because the raw materials were synthesized under S-rich conditions. The stoichiometric ratios of the nanosheets were determined using the XPS spectra. The atomic ratios of MoS_2 and WS_2 nanosheets were S/Mo = 1.973 and S/W = 1.842, respectively. According to ICP analysis in Section S11 (Supporting Information), the atomic ratios of MoS_2 and WS_2 nanosheets were S/Mo = 1.968 and S/W = 1.844, respectively. Those findings implied that the vacancy defects belonged to S-vacancies. Therefore, we conclude that the S-vacancy defects were generated during exfoliation because of the loss of sulfur atoms. There are two reasonable explanations for S-vacancy of MoS_2 and WS_2: (1) "Chemical weathering" exfoliation process: it is a force of crystallization to peel off MoS_2 and WS_2. In the exfoliation process, a small amount of Mo—S (W—S) bonds rupture can result in forming S-vacancy in the edge of MoS_2 or WS_2 and (2) obtained MoS_2 and WS_2 nanosheets are very thin layer, and their thickness are only 1–2 nm. In this case, the activity of nanosheets is higher than that of bulk MoS_2 and WS_2. Sulfur ions may produce hydrolysis reaction with water, such as $S^{2-} + 2H_2O \rightarrow H_2S + 2OH^-$. Thus, MoS_2 and WS_2 nanosheets surfaces contain large amounts of S-vacancy.

Atomic force microscopy (AFM) was used to determine the thickness of MoS_2 and WS_2 nanosheets, which were not observed in SEM and TEM characterization. Figure 2g shows single and flat MoS_2 nanosheets with a thickness of ≈1.3 nm (the corresponding AFM image is shown in Figure 2e). Similarly, the thickness of WS_2 nanosheets was ≈1.1 nm (Figure 2f,h). MoS_2 and WS_2 nanosheets obtained the single-layer thickness when the spacing between the nanosheets and basal was excluded.[32] Moreover, the sizes of MoS_2 and WS_2 nanosheets are similar to those observed in the SEM and TEM images (Figure S4, Supporting Information), and the sheets were very thin. This finding indicated that "chemical weathering" exfoliation is effective for peeling MoS_2 and WS_2.

The large band gaps of perfect MoS_2 and WS_2 monolayers are unsuitable for applications in laser saturable adsorption

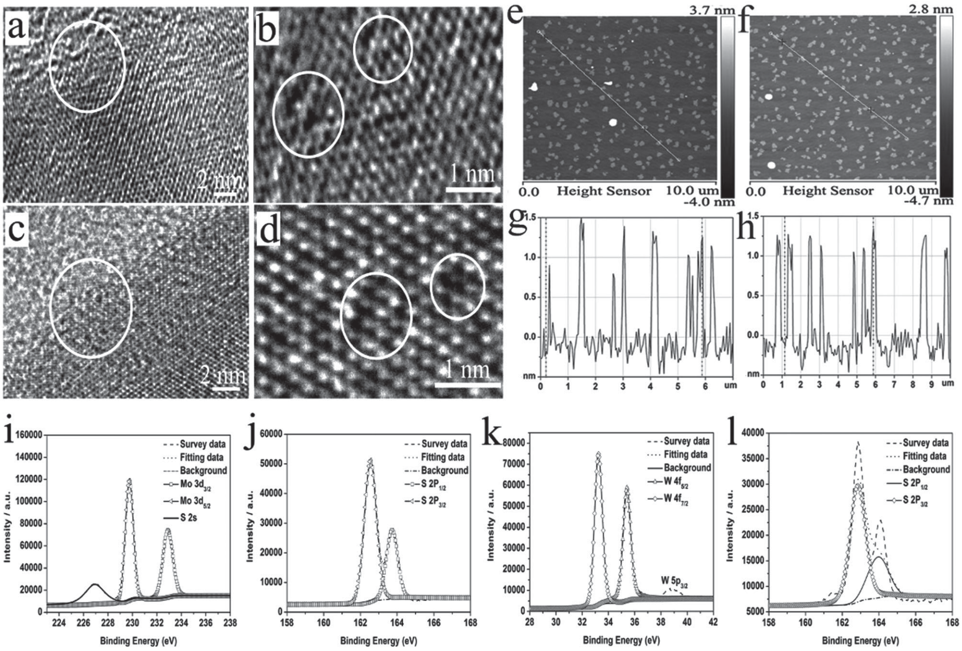

Figure 2. High-resolution TEM images of the edge and surface part of a,b) MoS_2 and c,d) WS_2 monolayers with vacancies and vacancy defect. e,f) AFM images and g,h) the corresponding height profiles of "chemical weathering" exfoliation of monolayer MoS_2 (left) and WS_2 (right) nanosheets. XPS spectra of MoS_2 and WS_2 monolayers, and the experimental measurement of S to Mo or W atomic ratio of MoS_2 and WS_2 nanosheets on mirror: i,j) Mo 3d, S 2s states, and S 2p states and k,l) W 4f, W 5p states, and S 2p states.

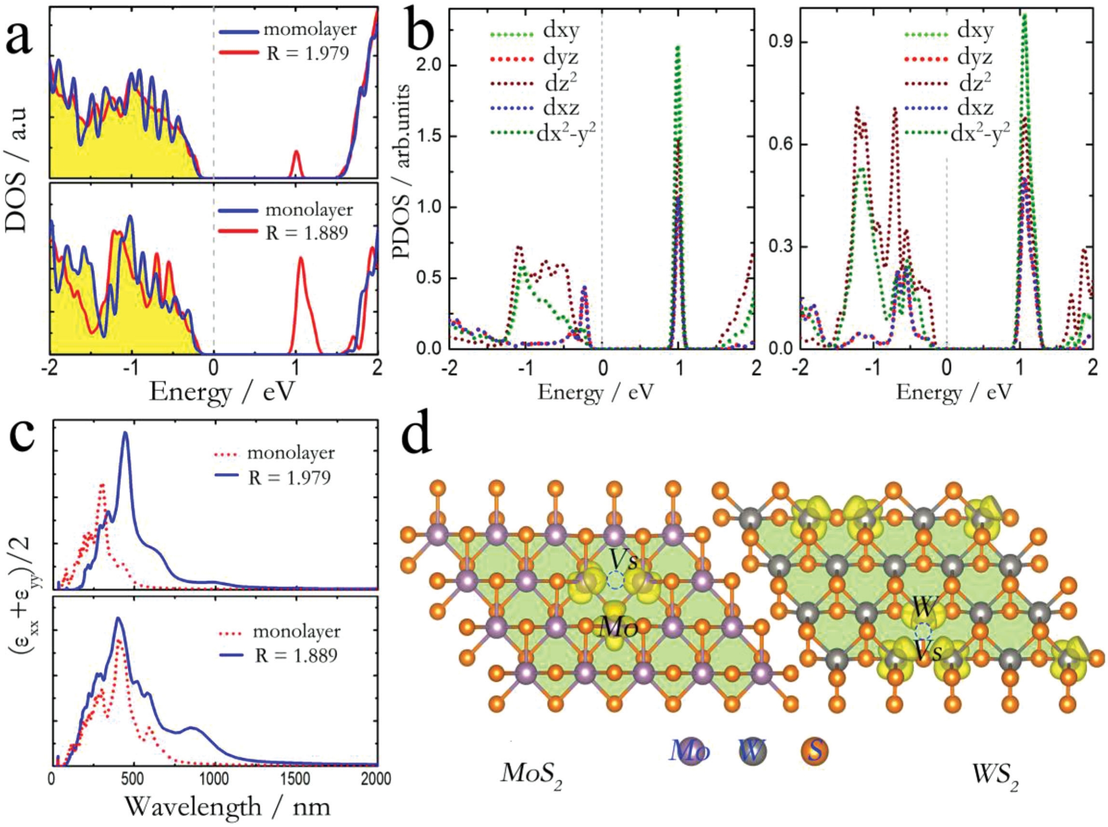

Figure 3. a) Electron density of states (DOS) of different models of MoS_2 (up) and WS_2 (down). b) The corresponding atomic orbital–resolved electron density of states (PDOS) projected on the dxy, dyz, dz^2, dxz, and dx^2–y^2 atomic orbitals of the Mo and W atoms nearest to the S-vacancy. The energy at the Fermi level is set to zero. c) The imaginary part of the isotropic dielectric function $((\varepsilon_{xx}(\omega)+\varepsilon_{yy}(\omega))/2)$ of 2D MoS_2 (up) and WS_2 (down) monolayers. d) The isosurfaces of the Kohn–Sham wavefunctions of the unoccupied intermediate states of S-vacancy with an isovalue of 0.03 Å^{-3}.

and mode locking. However, the presence of S-vacancy defects in TMDs may modify their electronic structures. We performed first-principles calculations to reveal the electronic structure modification of S-vacancy containing MoS_2 and WS_2 monolayers. The atomic ratios of the modes were set to S:Mo = 1.979 and S:W = 1.889, which are very close to the values of the real samples. Our theoretical calculations showed that the S-vacancy defects induced the intermediate states within the band gap as indicated by the electron density of state (DOS) shown in **Figure 3**a. The presence of the empty intermediate states reduced the band gap to 1.046 (MoS_2) and 1.008 eV (WS_2), which were suitable for achieving laser saturable adsorption and mode locking. The atomic orbital–resolved electron density of states (PDOS) projected on the Mo (or W) atoms nearest to the vacancy defects implies that the intermediate states mainly resulted from the dxy and dx^2–y^2 atomic orbitals of the transition metal atoms as shown in Figure 3b.

The roles of the intermediate states in the optical absorption properties of the S-vacancy containing MoS_2 and WS_2 monolayers were determined using first principles. The interactions between photons and electrons can be evaluated based on the electronic structures. We investigated the optical absorption properties by computing the complex dielectric function $\varepsilon(\omega) = \varepsilon_1(\omega) + i\varepsilon_{\alpha\beta}(\omega)$, in which the imaginary part $\varepsilon_{\alpha\beta}(\omega)$ reflects the optical absorption at a given frequency ω. The imaginary part $\varepsilon_{\alpha\beta}(\omega)$ can be written as[35,36]

$$\varepsilon_{\alpha\beta}(\omega)=\frac{4\Pi^2e^2}{\Omega}\lim_{q\to 0}\frac{1}{q^2}\sum_{c,v,\vec{k}}2w_{\vec{k}}\delta(\varepsilon_{c\vec{k}}-\varepsilon_{v\vec{k}}-\omega)\times\left\langle u_{c\vec{k}+e_\alpha\vec{q}}\,|\,u_{v,\vec{k}}\right\rangle\left\langle u_{c\vec{k}+e_\beta\vec{q}}\,|\,u_{v,\vec{k}}\right\rangle^{*} \tag{1}$$

where α and β represent the x-, y-, or z-coordinates, c and v refer to the conduction and valence band states, respectively, and $u_{c,\vec{k}}$ is the cell periodic part of the wavefunctions at the k-point. The data of $\varepsilon_{\alpha\beta}(\omega)$ over a wide frequency range can be used to calculate $\varepsilon_1(\omega)$ with Kramers–Kronig relationship. $\varepsilon_{\alpha\beta}(\omega)$ is decomposed into two components, namely, $\varepsilon_{zz}(\omega)$ and $(\varepsilon_{xx}(\omega)+\varepsilon_{yy}(\omega))/2$, which correspond to the electric field polarization along and perpendicular to the z-direction, respectively. We focused on the latter component because the laser radiates a transverse wave with a polarization perpendicular to the propagation direction.

The imaginary part of the isotropic dielectric function $((\varepsilon_{xx}(\omega)+\varepsilon_{yy}(\omega))/2)$ shown in Figure 3c showed the additional adsorption peaks at 997 (MoS_2) and 883 nm (WS_2) for the S-vacancy-containing monolayers compared with the corresponding perfect monolayers. This finding can be attributed to

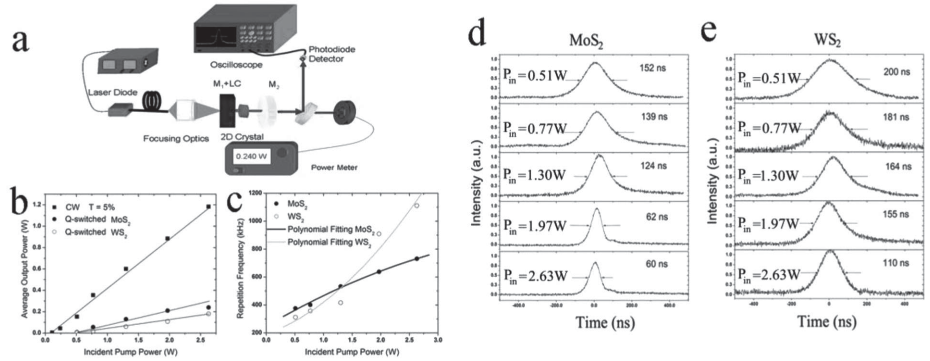

Figure 4. a) Experimental setup of MoS_2- and WS_2-based passively Q-switched $Nd:GdVO_4$ microchip lasers (LC: laser crystal $Nd:GdVO_4$; 2D crystal: atom-thick MoS_2 or WS_2). b) Average output power versus incident pump power. c) Repetition frequency versus incident pump power. d) MoS_2 and e) WS_2 of the pulse width versus incident pump power.

the excitation of electrons from the valence bands to the intermediate states. Therefore, the presence of the intermediate states strengthened the absorption of visible light. The density of the intermediate states in WS_2 monolayer was higher than that in MoS_2 monolayer because of the higher concentration of the S-vacancy defect. The optical adsorption of WS_2 monolayer for light with a wavelength of ≈940 nm was more remarkable than that of MoS_2 monolayer. These results suggested the feasibility of tuning electronic and optical properties to satisfy the requirements for laser saturable adsorption and mode-locking laser; tuning can be performed by engineering the intermediate states resulting from the S-vacancy defects in TMDs.

Considering the theoretical prediction, we prepared an MoS_2 or WS_2 passively Q-switched Nd^{3+}-doped microchip laser with a plano-concave cavity as shown in **Figure 4**a (the detailed information of this setup is introduced in Section S12 in the Supporting Information). Figure 4b shows that a maximum continuous-wave (CW) output power of 1.18 W was obtained under the incident pump power of 2.63 W with a slope efficiency (η_s) of 49.6% and an optical-to-optical efficiency (η_{o-o}) of 44.9%. In this experiment, the thickness of microchip gain medium was just 0.8 mm. Considering its end face sizes were 3 × 3 mm^2, in present end pumped configuration the water cooled area (i.e., the four side faces) was 35% of the total surface area. The relatively weak thermal diffusion ability led to the fracture of the gain medium when the incident pump power is higher than 3 W. So we kept the incident pump power below this level with a highest value of 2.63 W. The corresponding maximum CW output power was 1.18 W with a slope efficiency (η_s) of 49.6% and an optical-to-optical efficiency (η_{o-o}) of 44.9%, as shown in Figure 4b. With an MoS_2 saturable absorber inserted into the cavity, the passively Q-switching laser operation was realized when the incident pump power exceeded 0.51 W. The average output power almost linearly increased with the incident pump power. Under the largest pump power of 2.63 W, an average output power of 0.24 W was obtained which corresponded to η_s and η_{o-o} of 10.9% and 9.1%, respectively. For the WS_2 saturable absorber, a similar pump threshold of 0.51 W was observed under the same experimental conditions. The largest average output power was 0.18 W, resulting in η_s and η_{o-o} of 8.3% and 6.8%, respectively. Repetition frequency and pulse width were recorded with a 1 GHz oscilloscope (DPO 7104, Tektronix Inc.) connected to a fast photodiode, as shown in Figure 4c–e.

Figure 4d,e presents the pulse width of MoS_2 and WS_2 versus the incident pump power. The repetition frequency of MoS_2 Q-switching increased from 376 to 731 kHz, whereas the pulse width decreased from 152 to 60 ns (Figure 4d). The highest pulse energy and peak power were 0.33 μJ and 5.4 W, respectively. To our knowledge, this study is the first to achieve a Q-switched short pulse (<100 ns) by using a solid-state laser with monolayer MoS_2 nanosheets. The 60 ns pulse width reached the optimal level (56 ns) that we ever obtained in graphene, and is narrower than those of other 2D materials developed as Q-switchers this year; these 2D materials include graphene,[16] MoS_2,[26] Bi_2Te_3,[21] and Bi_2Se_3.[22] The repetition frequency of WS_2 Q-switching increased from 312 kHz to 1.11 MHz with a pulse width of 200–110 ns (Figure 4e). The corresponding highest pulse energy and peak power were 0.16 μJ and 1.5 W, respectively. To date, this setup is the first to reveal the infrared saturable absorption of monolayer WS_2 nanosheets through laser experiment.

Figure 5a shows the schematic of laser mode-locking experimental setup (the detailed introduction is shown in Section S12, Supporting Information). Figure 5b shows the mode-locked output power based on MoS_2 and WS_2 saturable absorber mirrors (SAM). Mode locking was observed at 0.51 W. The maximum output power of 0.772 and 0.828 W was obtained under 5.36 W absorbed pump powers for MoS_2 and WS_2, respectively. The slope and optical-to-optical efficiencies were 16.6% and 14.4% for MoS_2, respectively, and 18.2% and 15.4% for WS_2, respectively. In this experiment, the thickness of the laser gain medium was 6 mm. Considering its end face sizes were 3 × 3 mm^2, in our end pumped configuration the water cooled area (i.e., the four side faces) was 80% of the total surface area. The good thermal diffusion ability guaranteed that the laser gain medium could sustain high absorbed pump power larger than 10 W. Nevertheless, the 2D TMD saturable absorber in the cavity was damaged first at an absorbed pump power of 5.5 or so, and the corresponding laser damage threshold could be estimated to be ≈3.5 × 10^{-4} GW cm^{-2}, which was calculated from the intracavity laser intensity. So here we obtained the mode-locked results below the absorbed pump power of 5.5 W.

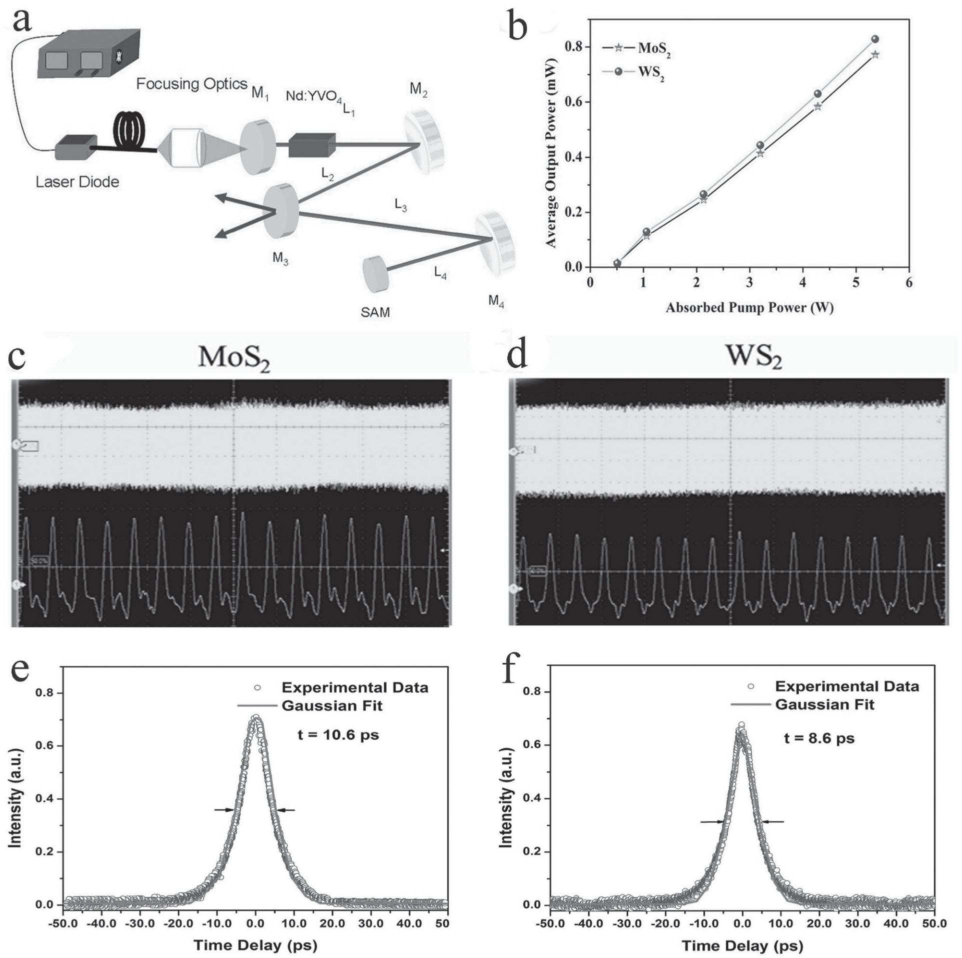

Figure 5. a) Schematic of laser mode-locking experimental setup. b) Average output power versus incident pump power of the Nd:YVO$_4$ mode-locked laser with respect to MoS$_2$ and WS$_2$ SAM. c,d) Mode-locked pulse trains for MoS$_2$ and WS$_2$ with a time spin of 1 µs (up) and 10 ns (down). e,f) Normalized autocorrelation pulse trace for 10.6 and 8.6 ps duration for MoS$_2$ and WS$_2$, respectively.

Figure 5c,d shows the mode-locked pulse trains measured under absorbed pump power of 5.36 W. The pulse trains recorded over 10 µs and 100 ns scales demonstrated the stability of the pulse trains. The pulse repetition was 155.9 and 158.9 MHz that corresponded to the pulse energies of 4.95 and 5.21 nJ, respectively. For the mode locking of MoS$_2$, the optimal average output power, single-pulse energy, pulse width, and peak power were 772 mW, 4.95 nJ, 10.6 ps (Figure 5e), and 467 W, respectively. As passively mode-locked material, this study is the first one to use MoS$_2$ in bulk solid-state lasers; most of these data are superior to those obtained from fiber lasers.[25,30] For example, the average output power, pulse width, peak power, single pulse energy, and pulse repetition were 5.1 mW, 1.28 ps, 480 W, 0.615 nJ, and 8.3 MHz, respectively, for an MoS$_2$ mode-locked fiber laser.[30] Comparing with these data, it can be seen that for the present MoS$_2$ mode-locked bulk crystal laser, except the pulse width is much broader, the single-pulse energy and pulse repetition rate increased by one order of magnitude, the average output power was improved by two orders of magnitude, while the peak power was at the same level. As for the mode locking of WS$_2$, the results were more satisfactory than those of MoS$_2$; the optimal average output power, single-pulse energy, pulse width, and peak power were 828 mW, 5.21 nJ, 8.6 ps (Figure 5f), and 606 W, respectively. From Figure 3c it can be seen that at 1 µm waveband WS$_2$ has exhibited larger imaginary part of the dielectric constant $((\varepsilon_{xx}(\omega) + \varepsilon_{yy}(\omega))/2)$ than MoS$_2$ does. It implies that WS$_2$ has larger absorption coefficient and modulation depth. The passively mode-locking theory has indicated that the pulse width is proportional to the factor $\Delta R^{-1/2}$, where ΔR is the modulation depth of the saturable absorber.[37] So a shorter pulse width (8.6 ps) was obtained from WS$_2$ than that (10.6 ps) from MoS$_2$. Besides, the average output power of WS$_2$ was also slightly larger (as shown in Figure 5b), which might be attributed to the higher pulse repetition rate caused by the resonator length, or the smaller nonsaturable absorption loss caused by the material preparation.

In summary, as newly developed saturable absorption materials, WS$_2$ and MoS$_2$ exhibit evident advantages in the preparation and excellent performance of Q-switching and mode locking. Hence, these materials present significant application potential in the optoelectronic field.

3. Conclusion

On the basis of the natural weathering exfoliation of seaside rocks, we propose a "chemical weathering" concept for exfoliation of atom-thick 2D materials from their bulk counterparts. We theoretically demonstrated that the proposed method is efficient for fabrication of TMD monolayers, such as MoS_2 and WS_2. These monolayers are difficult to prepare using other approaches. The proposed method also works well for other 2D materials, such as graphene and hexagonal boron nitride. The as-prepared MoS_2 and WS_2 monolayers exhibit excellent saturable adsorption and mode-locking properties in all-solid-state lasers because of the intermediate states resulting from the S-vacancy defects. Using MoS_2 or WS_2 monolayer as a saturable adsorption material, we achieved all-solid-state passively Q-switched laser operation with a pulse width of 60 ns. The obtained pulse width is lower, that makes the performance superior to those observed in other 2D materials. The ultrafast mode-locking results are also superior to those obtained in fiber lasers. Thus, the prepared monolayers are promising for all-solid-state laser applications.

4. Experimental Section

Preparation Method: MoS_2 and WS_2 were purchased from Alfa Aesar. Analytical-grade NaOH, cetyl trimethyl ammonium bromide, and alcohol were purchased from Sinopharm Chemical Reagent Co. Ltd. (Shanghai). All reagents were used as received.

In a typical experiment, 2 g of NaOH was dissolved in 10 mL of distilled water at 30 °C. Thereafter, 0.2 g of MoS_2 or WS_2 powder was dispersed in the solution under magnetic stirring at 30 °C. After several days, the solution was evaporated at 90 °C and a dry compound was obtained. After performing crystallization three times, the compound was washed and filtered. Finally, the product was divided into two equal parts: one part was dried at 80 °C for 12 h for characterization and the other part was dispersed in 20 mL of ethanol solution. The solutions were then centrifuged (1000 rpm for 30 min) to remove any aggregated sheets of MoS_2 or WS_2. The filtrates were stored in a small 20 mL bottle for MoS_2- and WS_2-based all-solid-state laser experiment (Section S12, Supporting Information).

The solubility of the exfoliated layered materials was determined as follows. The samples were dispersed in 20 mL of water (ethanol). The mixture was then sampled and centrifuged (1000 rpm for 30 min) to remove any aggregated sheets. The filtrates were placed in a small 20 mL bottle. The product was carefully collected by heating to remove the solvents and then vacuum dried overnight. Finally, the quality of the products was determined and the solubilities of the exfoliated layered materials were calculated (mg mL^{-1}).

Material Characterization: SEM was performed with a Hitachi S-4800 SEM. XRD patterns of the samples were recorded on a Bruker D8 Advance powder X-ray diffractometer using Cu Kα (λ = 0.15406 nm) radiation. UV–vis diffuse reflectance spectra of the samples were recorded on a Shimadzu UV-2550 spectrophotometer within a wavelength range of 200–900 nm. Raman spectra were obtained using the LabRam HR system from Horiba Jobin Yvon at room temperature with a 514 nm solid laser as the exciting source. HRTEM images were obtained with a Philips Tecnai 20U-Twin high-resolution TEM at an acceleration voltage of 200 kV. AFM 3100 Digital Instruments Dimension was used to investigate surface morphology, and X-ray photoelectron measurements were carried out using a monochromatized XPS spectrometer (a ThermoFisher ESCALAB 250) with AlKα radiation as the probe and a 500 mm analysis spot size. The base chamber pressure was 2×10^{-9} mbar.

Method and Computational Details: Ab initio calculations of the bulk and few-layer structures (one to four layers) were carried out using DFT with a projector augmented wave method and the Perdew–Burke–Ernzerhof (PBE) type generalized gradient approximation as implemented in the Vienna ab initio simulation package (VASP). The kinetic energy cutoff of the plane waves was set to 500 eV with the energy precision of 1×10^{-5} eV. The Brillouin zone was sampled using Γ-centered Monkhorst–Pack grids: $7 \times 7 \times 1$ for the monolayer materials and $7 \times 7 \times 5$ for the bulk materials. Test calculations showed that results are fully converged with respect to *k*-points. The atomic positions and the lattice vectors were fully optimized using the conjugate gradient (CG) scheme without any symmetric restriction until the maximum force on each atom was less than 0.005 eV Å^{-1}. The vdW interactions in MoS_2 are accounted for using a semiempirical correction to the Kohn–Sham energies when optimizing the bulk structures, while optimization of WS_2 structures are done at the PBE level since the semiempirical parameters for tungsten are currently not described by the dispersion potential.

Supporting Information

Supporting Information is available from the Wiley Online Library or from the author.

Acknowledgements

G.Z., S.H., and A.Z.W. contributed equally to this work. This work was supported by the National Basic Research Program of China (No. 2012CB932302), the National Natural Science Foundation of China (Contract Nos. 51321091, 61178060, and 91221101), Natural Science Foundation for Distinguished Young Scholar of Shandong Province (2012JQ18), and the National Super Computing Centre in Jinan. G.Z., X.P.H., and Y.Z.W. contributed in preparation, characterization, and analysis structure and performance of materials. S.H. and Z.P.W. contributed in laser test and analysis. A.Z.W. and M.W.Z. contributed in theoretical calculations. All the authors discussed the results and commented on the paper.

Note: This article was amended after its initial online publication. The middle initials were removed from the author names on September 2, 2015.

Received: May 13, 2015
Revised: July 6, 2015
Published online: July 28, 2015

---

[1] K. R. Paton, E. Varrla, C. Backes, R. J. Smith, U. Khan, A. O'Neill, C. Boland, M. Lotya, O. M. Istrate, P. King, T. Higgins, S. Barwich, P. May, P. Puczkarski, I. Ahmed, M. Moebius, H. Pettersson, E. Long, J. Coelho, S. E. O'Brien, E. K. McGuire, B. M. Sanchez, G. S. Duesberg, N. McEvoy, T. J. Pennycook, C. Downing, A. Crossley, V. Nicolosi, J. N. Coleman, *Nat. Mater.* **2014**, *13*, 624.

[2] K. S. Novoselov, V. I. Falko, L. Colombo, P. R. Gellert, M. G. Schwab, K. Kim, *Nature* **2012**, *490*, 192.

[3] K. F. Mak, K. He, C. Lee, G. H. Lee, J. Hone, T. F. Heinz, J. Shan, *Nat. Mater.* **2013**, *12*, 207.

[4] M. Lukoski, A. Daniel, F. Meng, A. Forticaux, L. Li, S. Jin, *J. Am. Chem. Soc.* **2013**, *135*, 10274.

[5] O. Lopez-Sanchez, D. Lembke, M. Kayci, A. Radenovic, A. Kis, *Nat. Nanotechnol.* **2013**, *8*, 497.

[6] W. Zhao, Z. Ghorannevis, L. Chu, M. Toh, C. Kloc, P. Tan, G. Eda, *ACS Nano* **2013**, *7*, 791.

[7] J. Song, J. Park, W. Lee, T. Choi, H. Jung, C. Lee, S. Hwang, J. Myoung, J. Jung, S. Kim, C. Lansalot-Matras, H. Kim, *ACS Nano* **2013**, *7*, 11333.

[8] A. L. Elías, N. Perea-López, A. Castro-Beltrán, A. Berkdemir, R. Lv, S. Feng, A. Long, T. Hayashi, Y. A. Kim, M. Endo, H. R. Gutiérrez,

N. R. Pradhan, L. Balicas, T. E. Mallouk, F. López-Urías, H. Terrones, M. Terrones, *ACS Nano* **2013**, *7*, 5235.

[9] K. Kosmider, J. Fernández-Rossier, *Phys. Rev. B* **2013**, *87*, 07545.

[10] T. Georgiou, R. Jalil, B. D. Belle, L. Britnell, R. V. Gorbachev, S. V. Morozov, Y. Kim, A. Gholinia, S. J. Haigh, O. Makarovsky, L. Eaves, L. A. Ponomarenko, A. K. Geim, K. S. Novoselov, A. Mishchenko, *Nat. Nanotechnol.* **2012**, *8*, 100.

[11] L. Britnell, R. M. Ribeiro , A. Eckmann, R. Jalil, B. D. Belle, A. Mishchenko, Y.-J. Kim, R. V. Gorbachev, T. Georgiou, S. V. Morozov, A. N. Grigorenko, A. K. Geim, C. Casiraghi, A. H. Castro Neto, K. S. Novoselov, *Science* **2013**, *340*, 1311.

[12] K. Wang, J. Wang, J. Fan, M. Lotya, A. O'Neill, D. Fox, Y. Feng, X. Zhang, B. Jiang, Q. Zhao, H. Zhang, J. Coleman, L. Zhang, W. Blau, *ACS Nano* **2013**, *7*, 9260.

[13] J. Zheng, H. Zhang, S. Dong, Y. Liu, C. T. Nai, H. S. Shin, H. Y. Jeong, B. Liu, K. P. Loh, *Nat. Commun.* **2014**, *5*, 2995.

[14] H. Zhang, S. B. Lu, J. Zheng, J. Du, S. C. Wen, D. Y. Tang, K. P. Loh, *Opt. Express* **2014**, *22*, 7249.

[15] D. Mao, Y. Wang, C. Ma, L. Han, B. Jiang, X. Gan, S. Hua, W. Zhang, T. Mei, J. Zhao, *Sci. Rep.* **2015**, *5*, 7965.

[16] H. Yu, X. Chen, H. Zhang, X. Xu, X. Hu, Z. Wang, J. Wang, S. Zhuang, M. Jiang, *ACS Nano* **2010**, *4*, 7582.

[17] Z. Sun, T. Hasan, F. Torrisi, D. Popa, G. Privitera, F. Wang, F. Bonaccorso, D. M. Basko, A. C. Ferrari, *ACS Nano* **2010**, *4*, 803.

[18] Q. Bao, H. Zhang, Y. Wang, Z. Ni, Y. Yan, Z. Shen, K. P. Loh, D. Tang, *Adv. Funct. Mater.* **2009**, *19*, 3077.

[19] Q. Bao, H. Zhang, Z. Ni, Y. Wang, L. Polavarapu, Z. Shen, Q. Xu, D. Tang, K. P. Loh, *Nano Res.* **2011**, *4*, 297.

[20] H. Yu, H. Zhang, Y. Wang, C. Zhao, B. Wang, S. Wen, H. Zhang, J. Wang, *Laser Photonics Rev.* **2013**, *7*, L77.

[21] Y. Chen, C. J. Zhao, S. Q. Chen, J. Du, P. H. Tang, G. B. Jiang, H. Zhang, S. C. Wen, D. Y. Tang, *IEEE J. Sel. Top. Quantum Electron.* **2014**, *20*, 0900508.

[22] Z. Q. Luo, C. Liu, Y. Z. Huang, D. D. Wu, J. Y. Wu, H. Y. Xu, Z. P. Cai, Z. Q. Lin, L. P. Sun, J. Weng, *IEEE J. Sel. Top. Quantum Electron.* **2014**, *20*, 0902708.

[23] J. Sotor, G. Sobon, K. M. Abramski, *Opt. Express* **2014**, *22*, 13244.

[24] H. Liu, A. Luo, F. Wang, R. Tang, M. Liu, C. Luo, W. Xu, C. Zhao, H. Zhang, *Opt. Lett.* **2014**, *39*, 4591.

[25] J. Du, Q. Wang, G. Jiang, C. Xu, C. Zhao, Y. Xiang, Y. Chen, S. Wen, H. Zhang, *Sci. Rep.* **2014**, *4*, 6346.

[26] S. Wang, H. Yu, H. Zhang, A. Wang, M. Zhao, *Adv. Mater.* **2014**, *26*, 3538.

[27] K. S. Novoselov, A. K. Geim, S. V. Morozov, D. Jiang, Y. Zhang, S. V. Dubonos, I. V. Grigorieva, A. A. Firsov, *Science* **2004**, *306*, 666.

[28] J. N. Coleman, M. Lotya, A. O'Neill, S. D. Bergin, P. J. King, U. Khan, K. Young, A. Gaucher, S. De, R. J. Smith, I. V. Shvets, S. K. Arora, G. Stanton, H. Kim, K. Lee, G. T. Kim, G. S. Duesberg, T. Hallam, J. J. Boland, J. J. Wang, J. F. Donegan, J. C. Grunlan, G. Moriarty, A. Shmeliov, R. J. Nicholls, J. M. Perkins, E. M. Grieveson, K. Theuwissen, D. W. McComb, P. D. Nellist, V. Nicolosi, *Science* **2011**, *331*, 568.

[29] N. Nicolosi, M. Chhowalla, M. G. Kanatzidis, M. S. Strano, J. N. Coleman, *Science* **2013**, *340*, 1226419.

[30] H. Xia, H. Li, C. Lan, C. Li, X. Zhang, S. Zhang, Y. Liu, *Opt. Express* **2014**, *22*, 17341.

[31] X. Li, X. Hao, M. Zhao, Y. Wu, J. Yang, Y. Tian, G. Qian, *Adv. Mater.* **2013**, *25*, 2200.

[32] M. Du, X. Li, A. Wang, Y. Wu, X. Hao, M. Zhao, *Angew. Chem., Int. Ed.* **2014**, *53*, 3645.

[33] Y. Zhang, Y. Zhang, Q. Ji, J. Ju, H. Yuan, J. Shi, T. Gao, D. Ma, M. Liu, Y. Chen, X. Song, H. Y. Hwang, Y. Cui, Z. Liu, *ACS Nano* **2013**, *7*, 8963.

[34] H. Matte, A. Gomathi, A. K. Manna, D. J. Late, R. Datta, S. K. Pati, C. N. R. Rao, *Angew. Chem., Int. Ed.* **2010**, *49*, 4059.

[35] M. Gajdoš, K. Hummer, G. Kresse, J. Furthmüller, F. Bechstedt, *Phys. Rev. B* **2006**, *73*, 045112.

[36] Z. Wang, M. Zhao, X. Wang, Y. Xi, X. He, X. Liu, S. Yan, *Phys. Chem. Chem. Phys.* **2012**, *14*, 15693.

[37] G. Herziger, H. Weber, R. Poprawe, *Laser Physics and Application*, Springer-Verlag, Berlin, Germany **2007**.